





Article

Experimental Investigation of a Hybrid Device Combining a Wave Energy Converter and a Floating Breakwater in a Wave Flume Equipped with a Controllable Actuator

Luca Martinelli ^{1,*}, Giulio Capovilla ¹, Matteo Volpato ¹, Piero Ruol ¹, Chiara Favaretto ¹, Eva Loukogeorgaki ² and Mauro Andriollo ³

¹ Civil, Environmental and Architectural Engineering (ICEA) Department, University of Padova, 35129 Padova, Italy; giulio.capovilla@studenti.unipd.it (G.C.); matteo.volpato@unipd.it (M.V.); piero.ruol@unipd.it (P.R.); chiara.favaretto@dicea.unipd.it (C.F.)

² Department of Civil Engineering, Faculty of Engineering, Aristotle University of Thessaloniki, 54124 Thessaloniki, Greece; eloukog@civil.auth.gr

³ Department of Industrial Engineering (DEI), University of Padova, Via Venezia, 1, 35131 Padova, Italy; mauro.andriollo@unipd.it

* Correspondence: luca.martinelli@unipd.it

Abstract: This paper presents a hydrodynamic investigation carried out on the “Wave Attenuator” device, which is a new type of floating breakwater anchored with piles and equipped with a linear Power Take Off (PTO) mechanism, which is typical for wave energy converters. The device is tested in the wave flume, under regular waves, in slightly non-linear conditions. The PTO mechanism, that restrains one of the two degrees of freedom, is simulated through an actuator and a programmable logic controller with preassigned strategy. The paper presents the system identification procedure followed in the laboratory, supported by a numerical investigation essential to set up a credible control strategy aiming at maximizing the wave energy harvesting. The maximum power conversion efficiency under the optimal PTO control strategy is found: it is of order 50–70% when the incident wave frequency is lower than the resonance one, and only of order 20% for higher frequencies. This type of experimental investigation is essential to evaluate the actual efficiency limitations imposed by device geometry.

Keywords: floating body hydrodynamics; hybrid wave energy converter; power take-off



Citation: Martinelli, L.; Capovilla, G.; Volpato, M.; Ruol, P.; Favaretto, C.; Loukogeorgaki, E.; Andriollo, M. Experimental Investigation of a Hybrid Device Combining a Wave Energy Converter and a Floating Breakwater in a Wave Flume Equipped with a Controllable Actuator. *Energies* **2024**, *17*, 40. <https://doi.org/10.3390/en17010040>

Academic Editors: Mehdi Neshat and Soheil Esmailzadeh

Received: 30 October 2023

Revised: 7 December 2023

Accepted: 9 December 2023

Published: 21 December 2023



Copyright: © 2023 by the authors. Licensee MDPI, Basel, Switzerland. This article is an open access article distributed under the terms and conditions of the Creative Commons Attribution (CC BY) license (<https://creativecommons.org/licenses/by/4.0/>).

1. Introduction

Ocean waves are an attractive renewable resource in view of their high energy density and good forecastability [1]. The first patents for devices to capture wave energy are more than 100 years old (see, for example, the French patent [2] or the Italian “Melchiorre” device [3]). However, due to the harsh marine environment, there are severe survivability and reliability issues [4]. Similarly, ocean waves generally have an irregular pattern and, furthermore, a very low frequency, posing several technological challenges in harvesting wave energy with high efficiency. This is demonstrated by the fact that, up to now, the average wave energy power production is negligible: globally, by 2020, the wave energy installations reached 24.9 MW, with 12.7 MW located in European sea basins [5].

The overall wave conversion efficiency is the combination of two steps: from the wave to mechanical energy and from mechanical energy to electricity [6]. The working principles relative to the former energy transformation are three [7]: wave activated body, overtopping and oscillating water column. These working principles, combined with the location (at the shore, nearshore, and offshore) and orientation with respect to wave direction (attenuator, terminator, or point absorber), form the basis for the wave energy classification system used since the early EU reports (e.g., WaveNet ERK5-CT-1999-20001). In this classification, the transformation between mechanical and electrical energy is not considered.

Electrical energy transformation is carried out using the so-called Power Take Off (PTO) mechanism/system. The PTO is essentially formed by a drive train, an electrical generator, a controller, and a series of ancillary equipment that also assures energy quality [8].

Scale effects do not enable the correct simultaneous representation of the transformation from wave to mechanical to electrical energies, accounting for all the interactions. When the device is scaled down to fit into the wave laboratory, the generator becomes so small that cannot be efficient (friction forces become proportionally too large). Early experiments, following a consolidated R&D roadmap [9], tend to focus on the wave to mechanical energy transformation, by modeling the interactions between “real” waves (generated in the wave tank) and the Wave Energy Converter (WEC) model, paying only a marginal attention to the PTO. Hence the electrical effects are not modelled. In [10], a real (large) PTO is used that does not fit into a small wave flume, and the PTO is excited by a six DOF industrial robot that moves the device as if it were under the wave action. Hence the wave to mechanical transformation is simulated but not directly modelled.

When the PTO is an oversimplified model, the interactions of the control strategy with the body dynamics (and the mooring system) cannot be considered and this oversimplification severely penalizes the initial phase of the development path [11]. The PTO mechanism impacts not only efficiency and costs but also the size and the reliability of the WEC, playing an essential role in the technological advancement of WECs.

In other experiments, greater attention is properly dedicated to the interactions with the PTO, following different approaches, aiming at finding the actual energy available for harvesting. For example, in [12] a sort of negative stiffness is used to modify the resonance frequency of the Weptos floater, thus implementing in practice what was envisaged in [11] in terms of a negative spring. In [13], the efficiency of the EP4 device is investigated at a small scale, by modeling the PTO as a resistive force combined with a latching mechanism in order to confine the velocity signal when the force is larger. In [14], the PTO system consists of a magnetic powder brake, able to produce different Coulomb damping forces or approximate Coulomb damping forces, and a current controller.

An even more detailed representation of the PTO control system is possible in larger scale experiments, e.g., [15–18]. In essence, the aim of those experiments is to first find the intrinsic impedance of the system $Z(\omega)$. Then, the optimal PTO load is defined by imposing the PTO impedance to be equal to $Z^*(\omega)$, which is the complex conjugate of the intrinsic impedance (see, for instance, [11]). Different strategies have been proposed to reach the best possible PTO load considering a number of impediments, such as excitation load prediction under irregular waves; wave nonlinearity; compliance with constraints on load, velocity, and excursion of the PTO and device survivability; reasonable limitation of the reactive load; and fatigue [19]. In presence of irregular waves, real-time estimates of the peak frequency and the energy of the wave excitation force are obtained by means of an (Extended) Kalman Filter, or through a relatively simple AR (Autoregressive) model that implicitly predicts the cyclical wave behavior [20].

The aim of this research is to investigate the performance of a hybrid device named “wave attenuator” that combines a WEC and a floating breakwater, through small-scale laboratory tests in the wave flume of Padova University, with a focus on the interactions between the WEC and the PTO. In fact, in the above experimental facilities, a controlled actuator able to mimic in small scale the PTO is available, which has enabled the investigation of the interactions between the power control system and the WEC hydrodynamic response since the early stages of WEC development.

The paper is organized as follows: Sections 2 and 3 describe, respectively, the Wave Attenuator device and the test setup. Section 3 defines the two DoF equation framework and the PTO constraints. Section 4 presents the tests for the identification of the intrinsic impedance of the system and the excitation force. Section 5 shows the tests with the control strategy. Then, in Section 6, conclusions are drawn.

2. The Wave Attenuator

The “Wave Attenuator” is essentially a floating breakwater formed by a row of modules, each consisting of a hollow rectangular-shaped frame. Seaward, each module is moored with two piles through a connection hinge that allows both vertical translation motion and rotation. Landward, the device movements are restrained by a controlled electromechanical linear generator arm, hinged diagonally at the pile base. The PTO is, in principle, a bar with permanent magnets inserted into (and restrained by) a cylinder with coils (the electromagnetic stator) fixed to the floater: when appropriately energized, the stator is an effective break that can slow the oscillatory movements of the floater and convert mechanical energy into electricity. In this case, the arm may be considered as the drivetrain of the PTO that transforms the floating breakwater into a WEC. An alternative system could be based on a recirculating ball screw, as in [21]. A scheme of the cross-section of the device is shown in Figure 1.

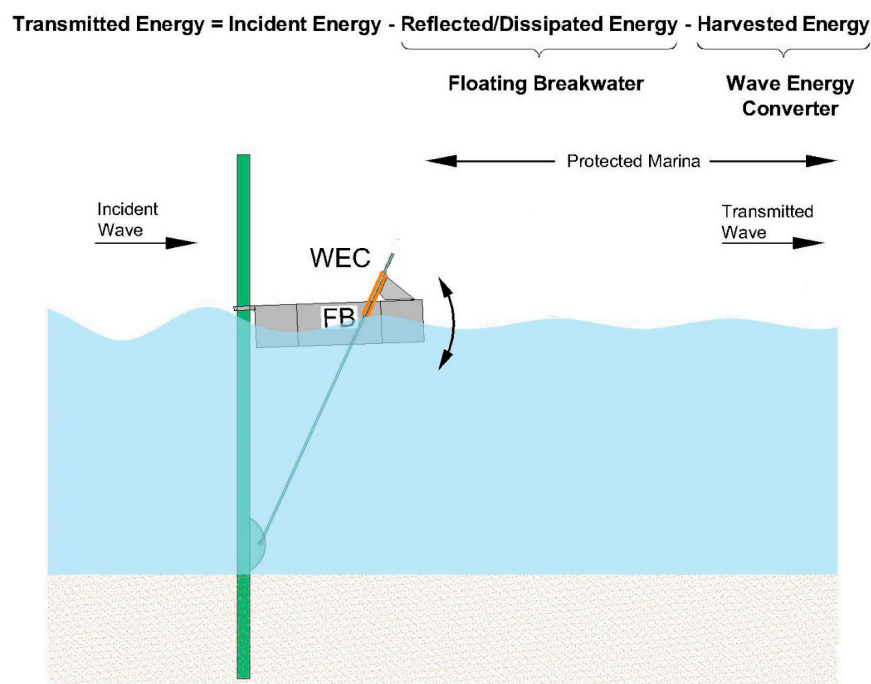


Figure 1. Scheme of the “wave attenuator” device.

The “wave attenuator” can be classified as a nearshore, terminator-type, wave activated body, since, respectively: (a) it is combined with a floating breakwater fixed with piles, (b) it is oriented parallel to the crest of the highest waves, and (c) it takes advantage of the relative movements of the floating structure and an oscillating rod, hinged at the base of the supporting piles.

WECs that have other purposes other than wave energy conversion are also called hybrids [13]. These devices may be called symbiotic if the energy harvesting provides an additional functional advantage, i.e., reducing the transmitted wave inside the marina [22]. The purpose of hybrid concepts [23] is to reduce the Levelized Cost of Energy (LCoE) by sharing the CAPEX and OPEX with other applications. Actually, the main purpose of the “Wave Attenuator” is marina protection, and not all modules are equipped with this system (only the most exposed ones). Hence, the shape of the Wave Attenuator is very different from the typical optimized shapes discussed (and reviewed) in [24–26].

Accordingly, the “wave attenuator” is symbiotic because the energy extraction mechanism increases the attenuation capacity of the floating breakwater, especially in the working conditions where the latter is otherwise less efficient (i.e., with long wave periods). More specifically, the “wave attenuator” has the potential to extend the range of applicability of floating breakwaters to also include locations where the design significant wave height is

between 1.0 m and 1.5 m and the peak period is between 3 and 4–4.5 s, if piles deployment is feasible. This can be an attractive solution, for example, for small fishery ports located in large lakes.

The Technological Readiness Level (TRL) of the examined device is four, justified by several lab tests that have been carried out at Padova University over the past 3 years. The preliminary test results are presented in [27].

The additional cost of placing a PTO only moderately increases the CAPEX and OPEX of the floating breakwater, so that, globally, there is a concrete possibility to have a low LCoE (with for example a payoff period of order 10 years in [28] and 20 years in [29]). The first issue is, however, to investigate the possible locations where the system can perform satisfactorily and, therefore, to assess the power production potential under different conditions [30].

3. Experimental Setup

The “Wave Attenuator” device has been modeled in the wave flume of Padova University in 1:20 scale. The wave flume is 36 m long, 1.0 m wide, with sides made of glass, and it is described, e.g., in [13,22].

The actuator (that mimics the presence of the PTO in small scale) is placed above water, for simplicity, and hinged to the side of the floater. Figure 2a shows the scheme of the “wave attenuator” model, while Figure 2b shows the floating module: 0.4 m wide, 0.1 m high, and 1.0 m long. The freeboard is equal to 3 cm and the gravity center is 2 cm below the mean water level. The module is made of aluminum and filled with closed cell polystyrene. Targets in black and white (Figure 2c), 2.0×2.0 cm, are used for video tracking when the position meters are not installed.

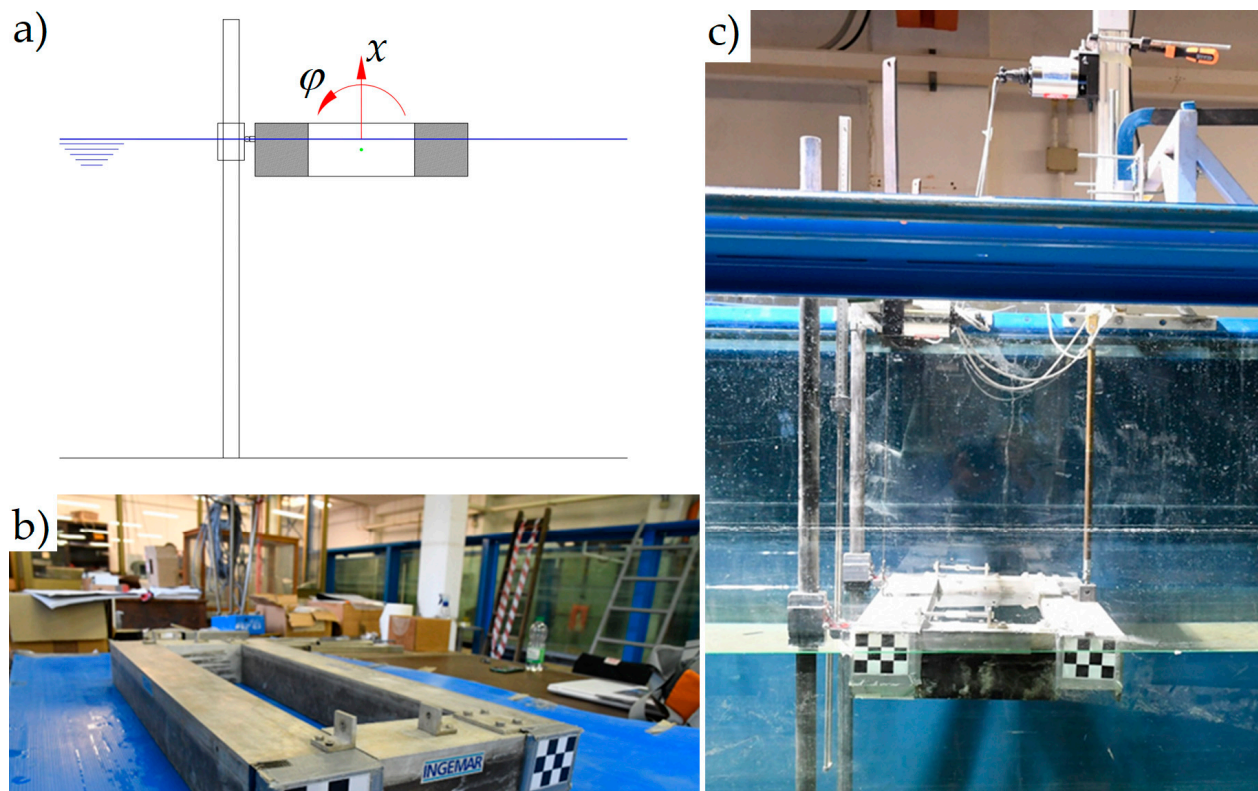


Figure 2. The “wave attenuator” device: (a) 2D sketch; (b) physical model; (c) view of the model in the wave flume.

The actuator (Figure 3) is controlled by a three-phase brushless motor, a PLC (Programmable Logic Unit) and some ancillary equipment (filters, resistance).

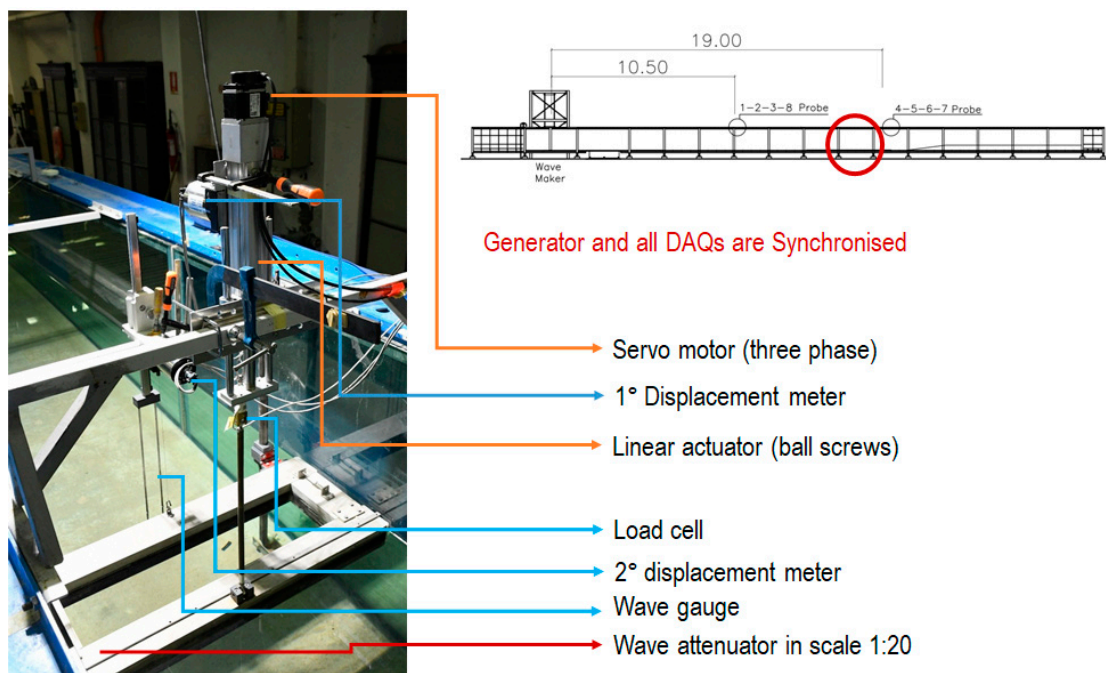


Figure 3. The controlling equipment and its location in the wave flume (top right). The red circle shows the position of the model in the wave flume.

The data acquisition system at 1 kHz is triggered and synchronized with the wave-maker. Irregular waves are run with the same seed, so that wave attacks can be identically reproduced. These measures ensure that loads in different configurations can be related to the same wave and, thus, allow to compare differences in both amplitude and phase.

Figure 4 shows the device from a different angle.

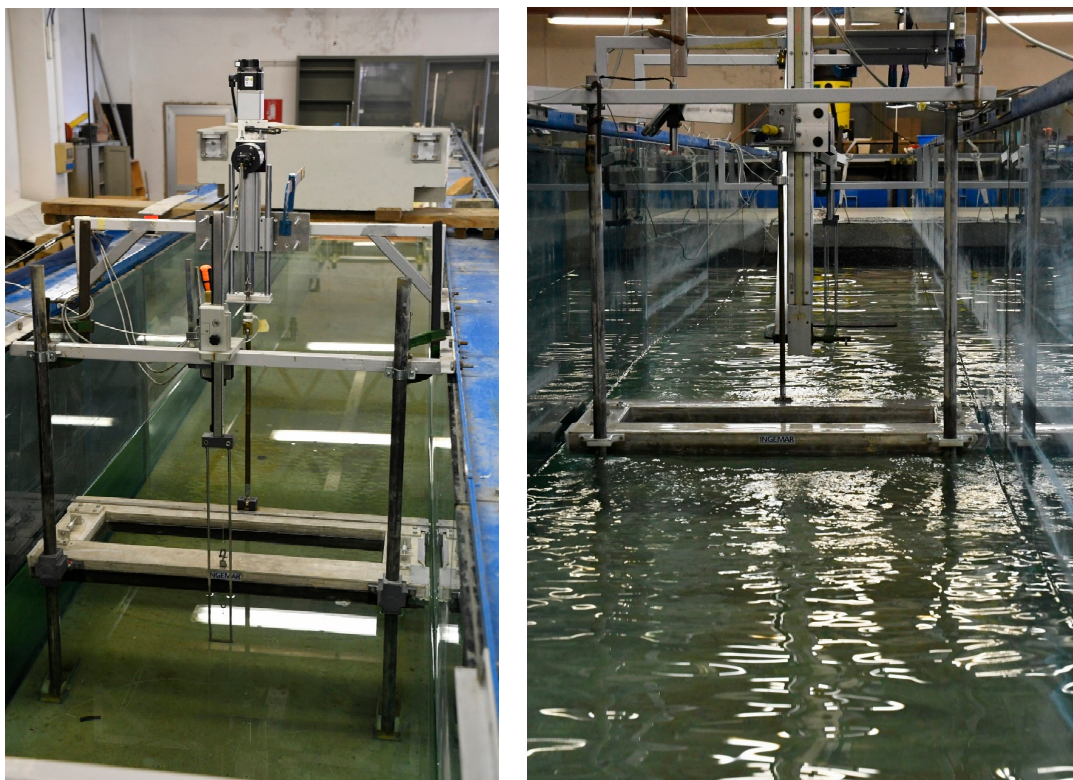


Figure 4. Images of the device in the wave flume.

4. System Identification

In order to identify the hydraulic response on the examined system (i.e., the “wave attenuator”), namely, the mechanical impedance, a combined numerical and experimental assessment approach is deployed. The experimental approach is considered more realistic and accurate, and the purpose of the simplified numerical model is merely to keep under control and interpret the experimental results.

The 2 DoF system hydrodynamics were modeled according to linear theory and through the Cummins equation. Forces and moments are computed assuming a frame placed at the free surface, in the middle of the structure, as a reference.

The symbols used for the 2 DoF, are φ for the rotation and x for the vertical oscillation. x is used instead of z to avoid confusion with the impedance, that is usually termed with the symbol $Z(\omega)$, with ω being the angular frequency. The center of the reference system is placed vertically at the water surface and horizontally at the center of the structure.

The transforms of φ and x are indicated in the following as $\varphi(\omega)$ and $X(\omega)$, while their use as subscripts denote the specific mixed terms. Force and torque are indicated by F and M , and the superscripts *pto* and *ex* clearly indicate the effect of the PTO (i.e., the actuator) and the external wave excitation. Hence, the system dynamics can be written as:

$$\begin{bmatrix} Z_{xx}(\omega) & Z_{x\varphi}(\omega) \\ Z_{\varphi x}(\omega) & Z_{\varphi\varphi}(\omega) \end{bmatrix} \begin{bmatrix} \dot{X}(\omega) \\ \dot{\varphi}(\omega) \end{bmatrix} = \begin{bmatrix} F^{ex}(\omega) \\ M^{ex}(\omega) \end{bmatrix} - \begin{bmatrix} F^{pto}(\omega) \\ M^{pto}(\omega) \end{bmatrix} \quad (1)$$

The generic impedance term can be written as:

$$Z_{ij}(\omega) = B_{ij}(\omega) + i \left(\omega(M_{ij} + A_{ij}(\omega)) - \frac{k_{ij}}{\omega} \right) \quad (2)$$

where the B_{ij} terms are the resistance radiative terms, including friction; M_{ij} and A_{ij} are, respectively, the mass and added mass terms; k_{ij} are the stiffness terms due to buoyancy and gravity; and subscripts i, j indicate the generic mixed terms.

It can be noticed that mixed terms that may couple the DoF equations derive from the possible friction that may arise at the hinge with the pile, and can be considered proportional to the horizontal reaction. In the model, this coupling is minimal.

Even in the absence of coupling, the apparent center of rotation of the structure when it moves under the waves action is not in the middle (i.e., during the tests, the structure does not rotate around the middle). In fact, the incident wave applies a nonsymmetric torque, which induces nonsymmetric rotation. It is easy to verify, by inserting in Equation (1) a proportionality between the vertical oscillation and rotation, namely $X(\omega) = b(\omega)\varphi(\omega)$ (where $b(\omega)$ is the center of rotation), that $b(\omega)$ is not zero in general and it is given by the following equation:

$$b(\omega) = \frac{Z_{\varphi\varphi}(\omega) F^{ex}(\omega)}{Z_{xx}(\omega) M^{ex}(\omega)} \quad (3)$$

4.1. Numerical Assessment

A preliminary assessment of the impedance is conducted numerically in the frequency domain. Since this assessment aims at supporting the interpretation of the experimental results, the frequency domain analysis has been conducted assuming an isolated floating body (i.e., the presence of the flume side walls is not taken into account).

In principle, the presence of the side walls poses a problem due to the small gap between the device and the side glass. More advanced CFD investigations (see, for example, [31–33]) are certainly more suited to simulating the experimental values with accuracy, but the deployment of tools are beyond the scope of the present study. The applied numerical approach relies on the conventional Boundary Integral Equation Method (BIEM), which is numerically realized using WAMIT © software [34]. The relevant analysis is based on a three-dimensional linear potential theory, where the device is also assumed to

oscillate freely along the vertical direction and around the hinge connection. Therefore, all degrees of freedom of the device, except the ones corresponding to heave and pitch, are considered restricted. The fluid is assumed inviscid and incompressible, while the flow is assumed irrotational. Consequently, the fluid motion is described in terms of the velocity potential, satisfying the Laplace equation. In addition to the Laplace domain equation, the boundary value problem is composed by the linearized free surface condition, the finite-water depth bottom boundary condition and the Neumann body condition on the wetted area of the device [34]. The boundary integral equations for the unknown diffraction and radiation potentials on the boundary of the floating body are formed by utilizing Green's theorem. The corresponding boundary value problem is, then, solved based on a three dimensional low-order panel method [34,35] and, subsequently, heave and pitch exciting forces and hydrodynamic coefficients are calculated. In [36] the accuracy of the typical linear potential flow model (termed LPF1 in that paper) is compared to more accurate models and to physical model tests for a floating sphere, and a noticeable error is found only for large displacements.

The geometrical characteristics of the device coincide with those of the experimental model. To achieve adequate computational accuracy, also considering the existence of an internal free surface (moon pool) in the interior region of the device, a quite dense mesh has been used including 2765 panels for modelling one half of the floating body's the wetted surface. The local coordinate system, which coincides with the global one, is taken on the free surface at the hinge connection. Accordingly, all physical quantities related to pitch are obtained with respect to the rotation point of the device. The water depth is taken equal to 0.6 m, while we consider the action of unit amplitude regular waves with frequencies varying between 0.1 rad/s and 12 rad/s with a 0.1 rad/s step. Figure 5 shows some indicative results obtained from the aforementioned frequency domain analysis. The existence of distinctive features (i.e., sharp peaks and/or local minima around zero and/or intense discontinuities) in the variation of the heave exciting force and hydrodynamic coefficients at high frequencies results from resonance of water motion modes in the rectangular cavity.

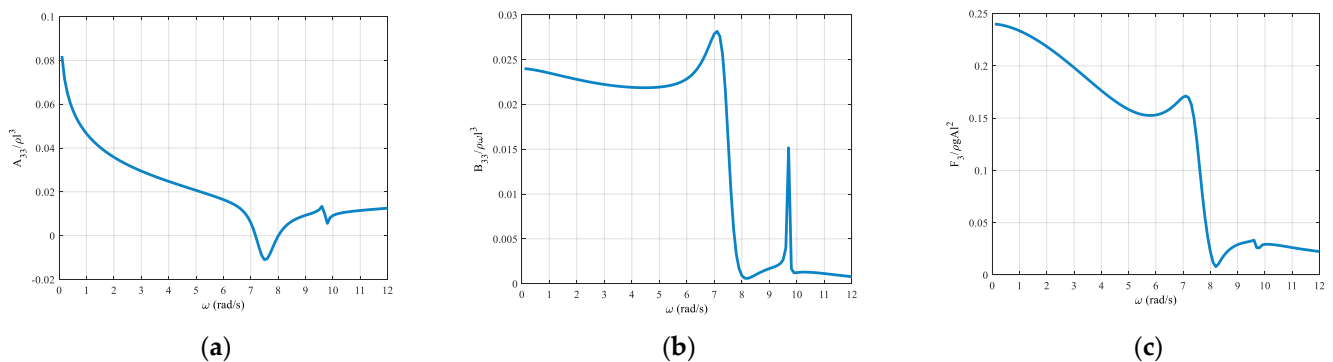


Figure 5. Frequency-domain (BIEM) numerical analysis results for the heave motion: (a) nondimensional added mass; (b) nondimensional radiation damping; (c) nondimensional excitation force (on the vertical axis, $l = 1$ m, and A is the wave amplitude).

Similarly, a simple standard approach was used for the real-time simulations. They are based on the solution of the Cummins equation with 2DoF. The convolution term is solved through a simple direct integration, limiting the duration of the time window to 12 s, of which 2 s are relative to the part of the signal ahead of time (Figure 6). A standard Kalman filter is used to anticipate the force signal ([37]).

To achieve a sufficiently accurate time-domain simulation (through the Cummins equation), a sufficiently small time-step was required. The result achieved with $dt = 0.001$ s may be verified in Figure 7, where the RAO induced by incident regular waves of different frequencies is compared to the frequency-domain solution. Small differences are attributed to the approximations in the time-domain model.

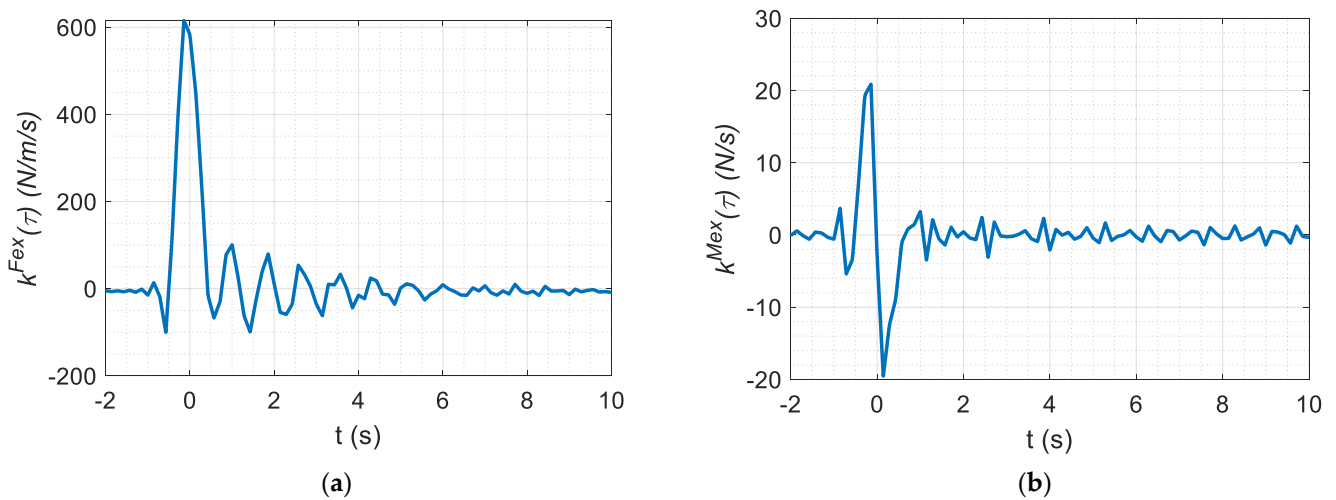


Figure 6. Indicative (a) excitation force and (b) torque used for real-time simulations. The force/torque is found as a time convolution of the above signals and the incident wave elevation.

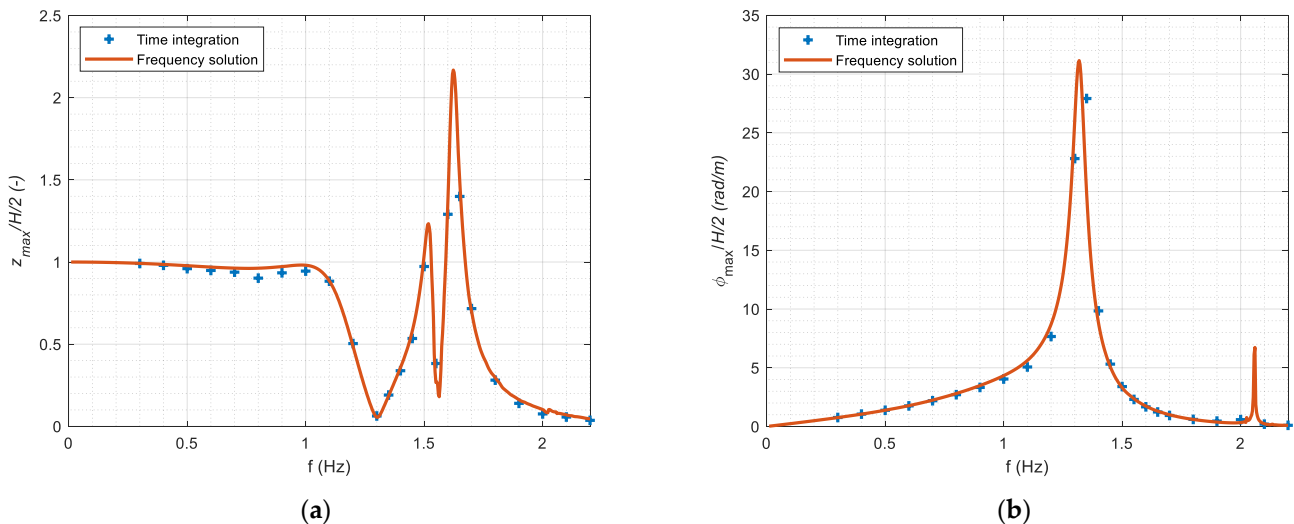


Figure 7. RAO of (a) the vertical force and (b) the rotation (with no additional damping).

The input parameters used in the numerical models are given in Table 1. It is noted that no additional friction is used to obtain the numerical results. It is expected, however, that the real damping matrix is larger, in order to represent the viscous dissipation and hence the actual experimental RAO. The damping matrix is calibrated using two coefficients in the diagonal terms, equal to 50 N s/m and 0.02 N m s/rad.

4.2. Experimental Assessment

The experimental investigation aims at defining the response of the system in the frequency domain, linearized at different levels of wave intensity. The “free tests”, the “forced oscillation tests”, and the “diffraction tests” are 180 s long, with an acquisition frequency of 1 kHz. Logging is triggered by the wave paddle.

The free tests are carried out in the absence of the linear actuator, with the purpose of investigating the wave transmission performance of the floating breakwater alone. Table 2 shows the test matrix for the diffraction tests.

For the purpose of this research, the tests allow to check the correspondence between the observed and theoretical position of the rotation center (Equation (3)), computed in absence of friction (Figure 8). Significant mismatches are found, especially for small waves and high frequencies, where the friction due to the pile has a larger influence.

Table 1. Model characteristics.

Parameter	Description	Value
M	Mass	12.5 kg
I	Inertia around midpoint at msl	0.35 kg m ²
A	Area intersecting the free surface	0.24 m ²
I_o	Inertia of area at msl around rotation axis (O)	0.0048 m ⁴
H_c	Depth of uplift center pressure	0.028 m
H_g	Depth of center of gravity	0.020 m
MC	Metacenter height (above water)	0.380 m
$A_{xx}(\infty)$	Added mass at infinite frequency ¹	16.88 kg
$A_{\phi\phi}(\infty)$	Added inertia at infinite frequency ¹	0.28 kg m ²
d	Water depth	0.600 m
Fr	Freeboard	0.030 m
ρ	Water density	1000 kg/m ³
k_z	Stiffness to vertical motion	2.35 kN/m
k_ϕ	Stiffness to pitch (around O)	43.41 kN m/rad

¹ According to WAMIT simulations.

Table 2. Characteristics of the diffraction tests. H = target incident wave height (X = test is done).

H	0.5 s	0.7 s	0.8 s	0.9 s	1.0 s	1.2 s	1.5 s	2.0 s
1 cm	X	X	X	X	X	X		
2 cm	X	X	X	X	X	X	X	X
3 cm			X	X	X	X	X	X
5 cm					X	X	X	X

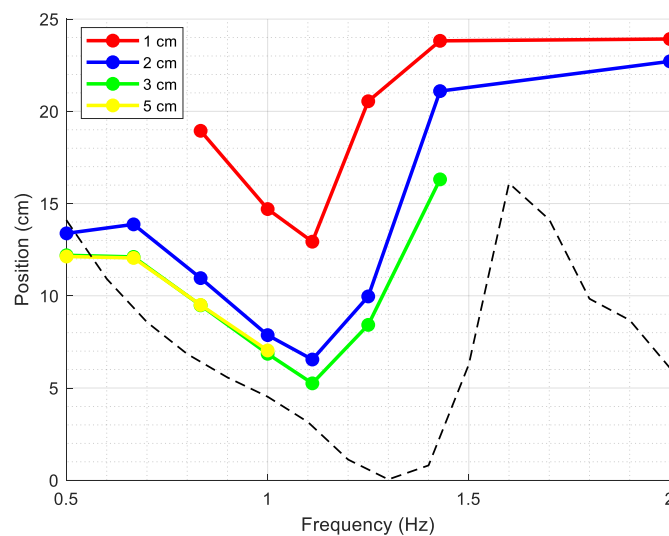


Figure 8. Horizontal position of the center of rotation $b(\omega)$ -Dotted line is obtained using Equation (3).

The forced oscillation tests are carried out in the absence of waves (Figure 9), moving the actuator sinusoidally according to the characteristics given in Table 3, and measuring the movements of the two extremes and the applied force through the load cell in line with the actuator.

Table 3. Characteristics of the forced oscillation tests. A = amplitude of the forced oscillation of the actuator. (X symbols indicate which tests are done).

A	0.5 s	0.7 s	0.8 s	0.9 s	1.0 s	1.2 s	1.5 s	2.0 s
1 cm	X	X	X	X	X	X		
2 cm	X	X	X	X	X	X	X	X
3 cm			X	X	X	X	X	X
5 cm					X	X	X	X

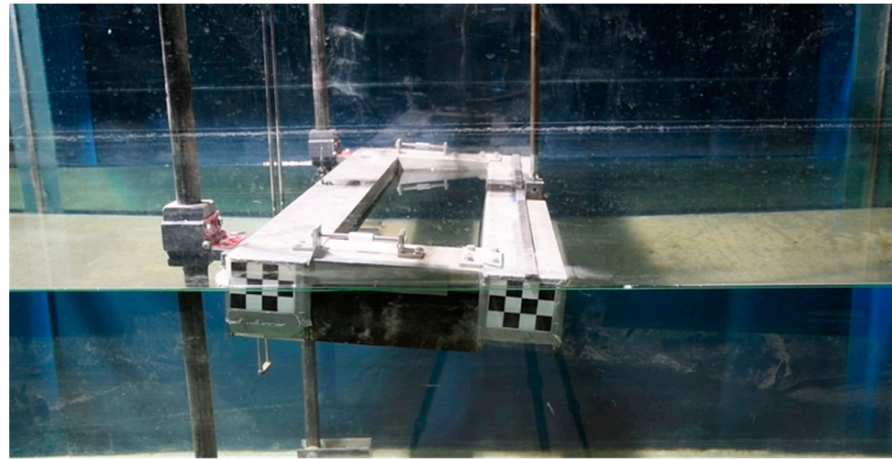


Figure 9. Forced oscillation tests.

Since tests are carried out in the absence of waves, there is no external force, and the only unknowns in Equation (1) are the two diagonal values of the impedance matrix. From a numerical point of view, the values of the impedance for each angle frequency and wave height are obtained by selecting the stable part of the measurements and carrying out a correlation with a sinusoidal signal. The results are given in Figures 10 and 11. They are relative to the frequency range 0.5–2 Hz.

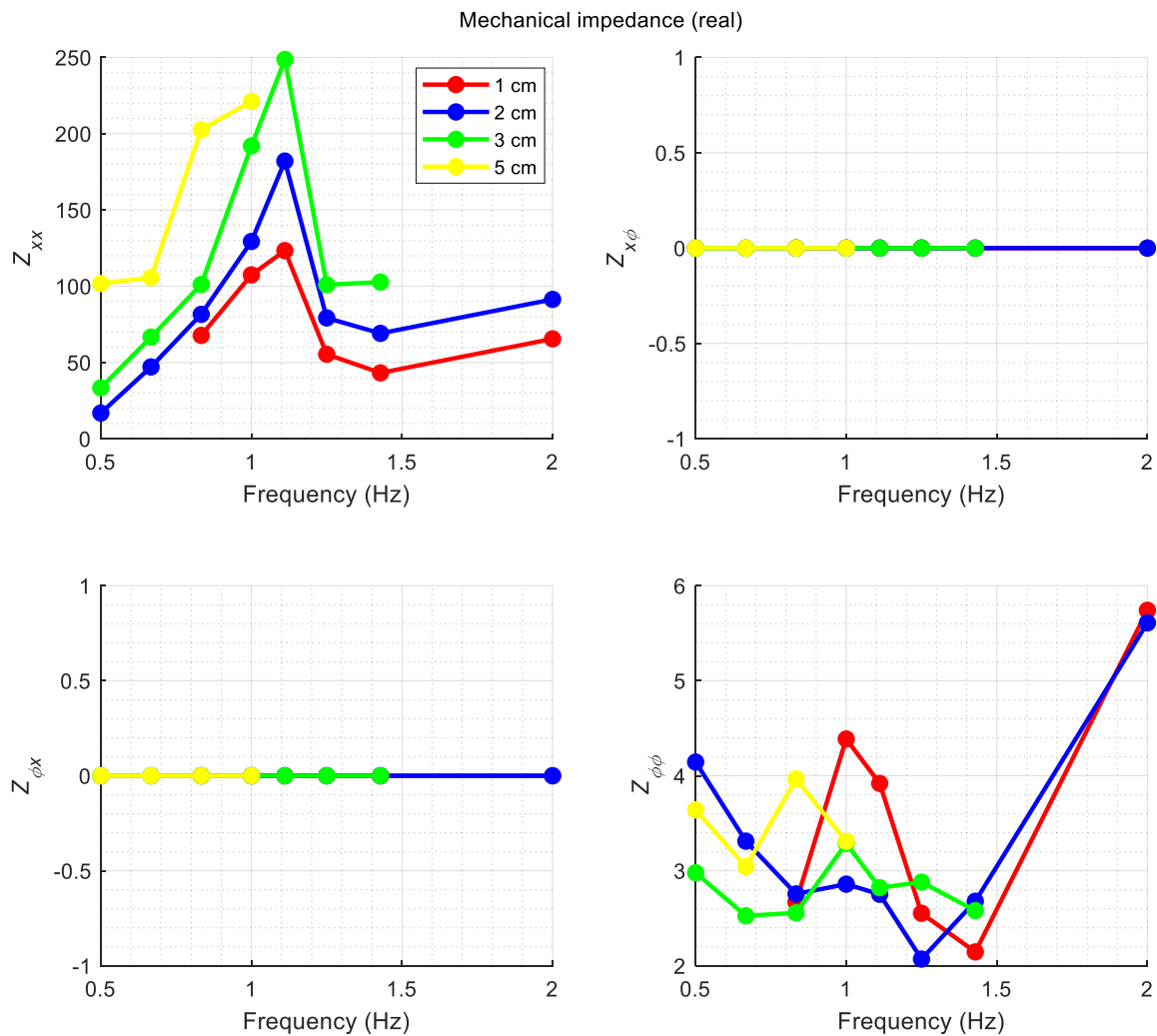


Figure 10. Experimental values of the real part of the mechanical impedance.

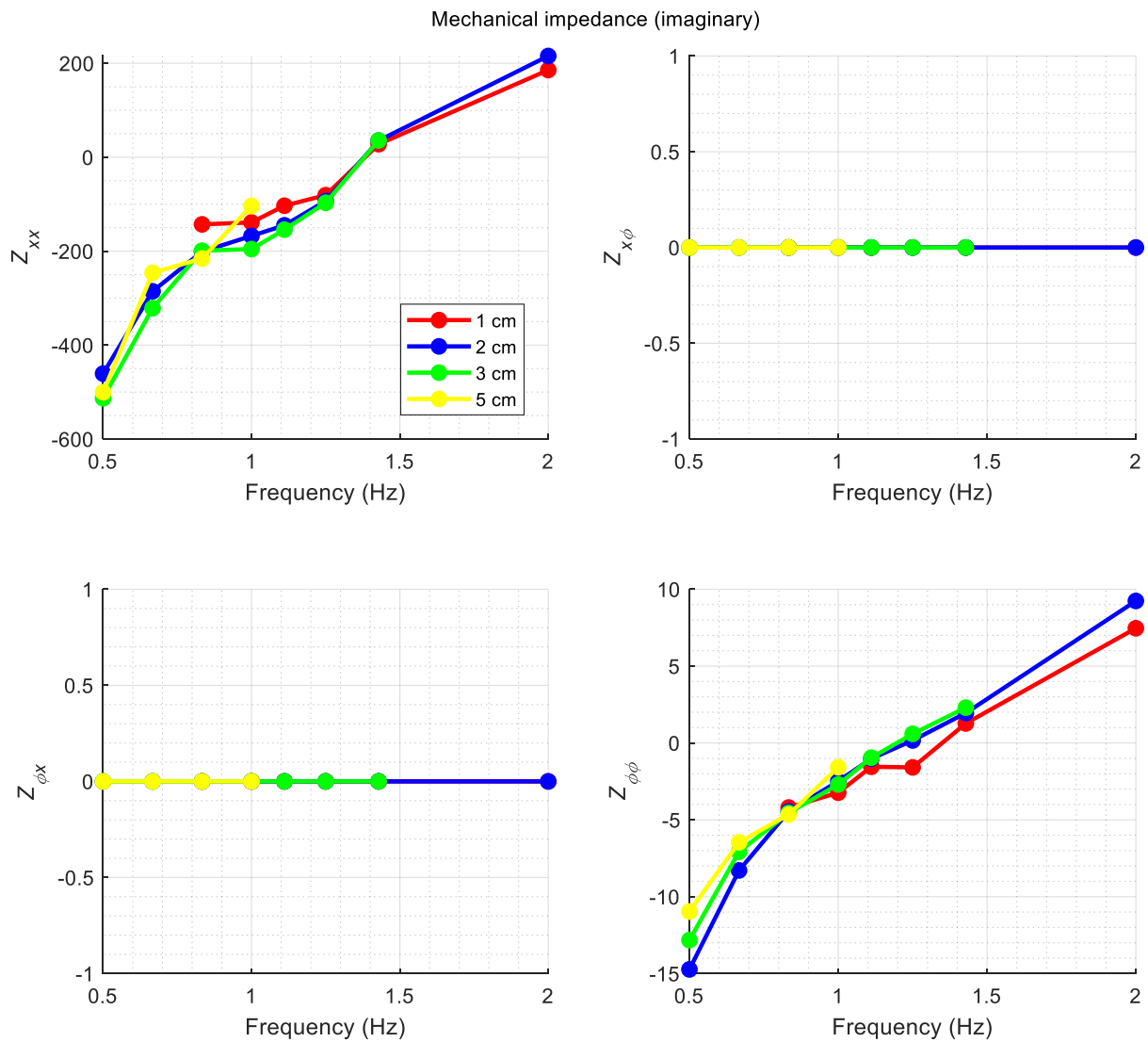


Figure 11. Experimental values of the imaginary part of the mechanical impedance.

The results clearly show a strong dependence with frequency, as expected. Unsurprisingly, the real part of the mechanical impedance, associated to dissipation, is more affected by the amplitude of the oscillations, whereas the imaginary part is less sensitive to it. This trend is similar but not exactly equal to the numerical assessment. Figure 12a,b show a comparison between the added mass and radiation matrices obtained from the simulations and the experimental values. In Figure 12a,b, for each frequency, the averages of the different experimental values (relative to different wave heights) are shown, as they seem to better fit the comparison. Nevertheless, the significant differences prove that the added value of the experimental research is considerable.

This numerical assessment was also used to find the reference values (highlighted by the circle in Figure 12) of the added mass and radiation damping at “zero frequency”. These values, considered equal for all wave heights, could be used to extrapolate the experimental impedance to frequencies lower than 0.5 Hz. With this precaution, it is possible to derive (by inverse Fourier transform) an impulsive response of desired duration (much longer than 2 s).

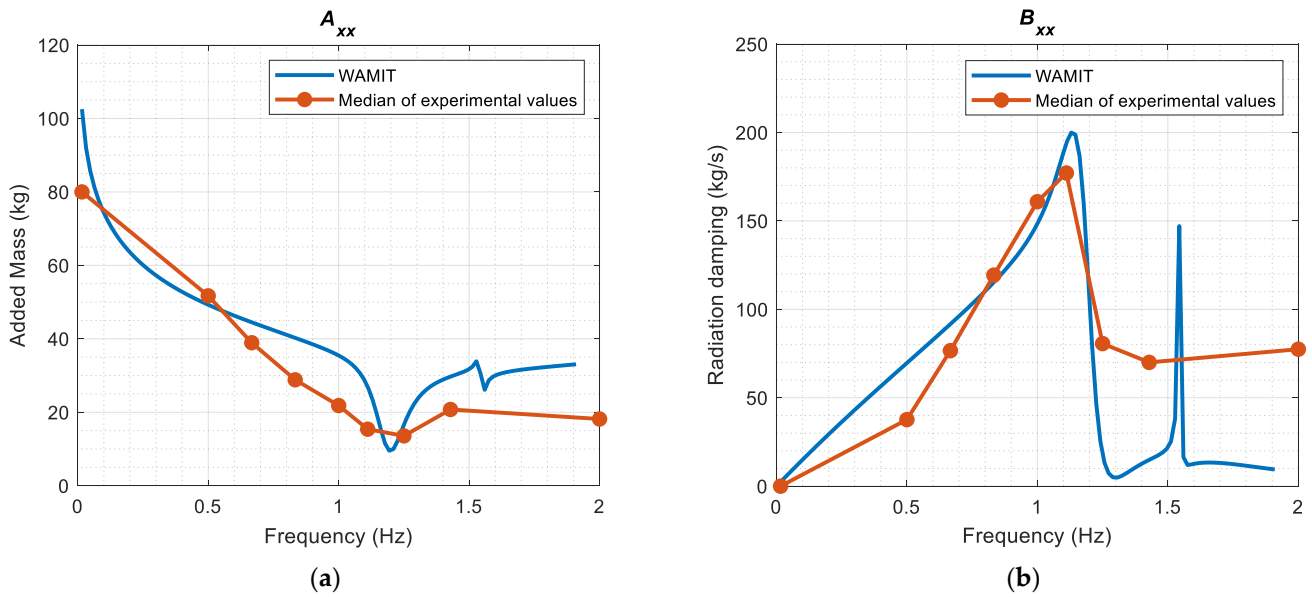


Figure 12. Average experimental values of heave: (a) added mass and (b) radiation damping compared to WAMIT.

5. Maximum Efficiency

The optimal reactive control induces resonance conditions in order to extract the maximum possible power. The magnitude of the PTO force is related to the real part of the mechanical impedance (see, for example, [11]), i.e., to the hydrodynamic resistive radiation matrix (or radiation damping), including dissipation effects.

For the particular position of the PTO in this setup, the transformed power is:

$$\langle P(\omega) \rangle = \langle F^{pto}(\omega) \dot{X}_{pto}(\omega) \rangle \quad (4)$$

where \dot{X}_{PTO} is the velocity of the point where the PTO is attached, shifted to the right of the reference system of half the structure width w ($w = 0.4$ m) and is hence given by:

$$\dot{X}_{pto} = \dot{X} + \frac{w}{2} \dot{\varphi} \quad (5)$$

The definition of the maximum oscillation amplitude is not trivial. Usually, it is easy to see that the maximum oscillation occurs at resonance conditions, which can be reached separately by heave and pitch. However, those motions are not in phase. At resonance, the heave and pitch velocities are in phase with the excitation force and torque, which, as shown in Figure 13, are not expected to be always in phase, according to the numerical simulations. In particular, below (approximately) 1.2 Hz, the two components are in phase quadrature (90° shift), whereas above this threshold, they are in phase. The relative importance of the two contributions is given in Figure 13, where the blue line is the first term in Equation (5); the heave oscillation, giving a lower contribution compared to the red line, is the second term in Equation (5), related to pitch.

The curves in Figure 14, representing the oscillations velocities at resonant conditions, are obtained as:

$$|\dot{X}(\omega)| = \frac{F^{ex}(\omega)}{2 \operatorname{Real}(Z_{xx}(\omega))} \quad (6)$$

$$\left| \frac{w}{2} \dot{\varphi}(\omega) \right| = \frac{M^{ex}(\omega)}{2 \operatorname{Real}(Z_{\varphi\varphi}(\omega))} \quad (7)$$

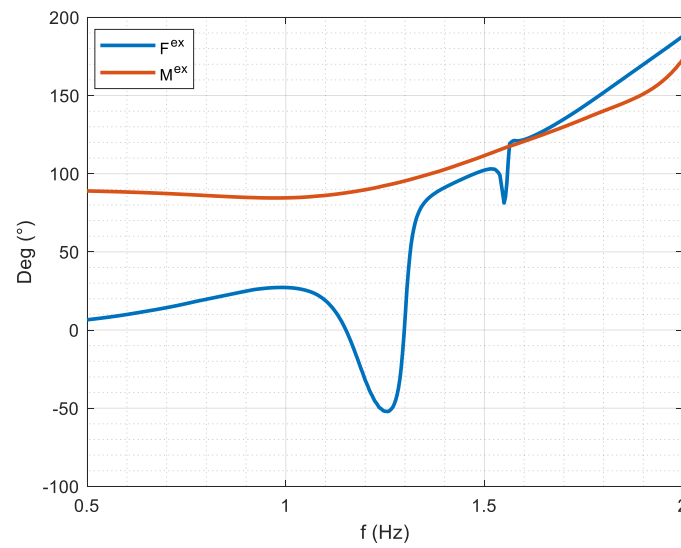


Figure 13. Expected phase lag between excitation force and torque with respect to the incident wave.

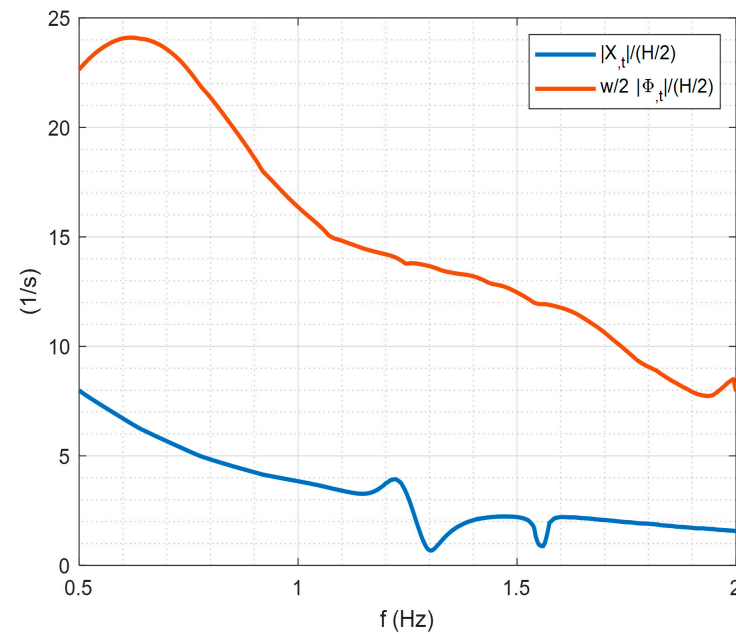


Figure 14. The vertical velocity amplitude at the PTO of the velocity per unit wave amplitude.

The force in PTO is given by:

$$F_3^{pto}(\omega) = \left[B_{pto} - j \frac{C_{pto}}{\omega} \right] \dot{X}_{pto}(\omega) \tag{8}$$

where the first term between the brackets is the PTO impedance $Z_{pto}(\omega)$ that requires optimization. The condition for maximum average power P is given by the maximization of:

$$\langle P \rangle = \langle B_{pto} | \dot{X}_{pto}(\omega) \dot{X}_{pto}(\omega) | \rangle \tag{9}$$

In a single DoF, the optimal impedance is the conjugate of the mechanical impedance. Therefore, since pitch oscillation is predominant compared to vertical oscillation, it may be expected that the optimal impedance $Z_{pto}(\omega)$ is close to the conjugate of $Z_{\varphi\varphi}(\omega)$. Numerically, the actual optimum value is obtained by a numerical procedure, where the values of $B_{pto}(\omega)$ and $C_{pto}(\omega)$ vary.

Note that two computations can be carried out, by assuming that the mechanical impedance is either the theoretical one (i.e., as obtained by WAMIT), or the experimental one. Considering that the vertical PTO force $F_3^{pto}(\omega)$ is applied in the corner, the PTO also applies a torque $\frac{w}{2}F_3^{pto}(\omega)$. Inserting these into Equation (1), we can easily derive the expression that describes the movements of the point where the PTO is attached:

$$\dot{X}(\omega) = \frac{1}{Z_{xx}(\omega)} \left[F^{ex}(\omega) - Z_{pto}(\omega) \dot{X}_{pto}(\omega) \right] \quad (10)$$

$$\dot{\varphi}(\omega) = \frac{1}{Z_{\varphi\varphi}(\omega)} \left[M^{ex}(\omega) - \frac{w}{2} Z_{pto}(\omega) \dot{X}_{pto}(\omega) \right]$$

$$\dot{X}_{PTO}(\omega) = \frac{1}{Z_{xx}(\omega)} \left[F^{ex}(\omega) - Z_{pto}(\omega) \dot{X}_{pto}(\omega) \right] + \frac{w}{2} \frac{1}{Z_{\varphi\varphi}(\omega)} \left[M^{ex}(\omega) - \frac{w}{2} Z_{pto}(\omega) \dot{X}_{pto}(\omega) \right]$$

$$\dot{X}_{PTO}(\omega) = \left[1 + \frac{Z_{PTO}(\omega)}{Z_{xx}(\omega)} + \left(\frac{w}{2} \right)^2 \frac{Z_{PTO}(\omega)}{Z_{\varphi\varphi}(\omega)} \right]^{-1} \left(\frac{F^{ex}(\omega)}{Z_{xx}(\omega)} + \frac{w}{2} \frac{M^{ex}(\omega)}{Z_{\varphi\varphi}(\omega)} \right) \quad (11)$$

By inserting Equation (11) into Equation (9), the expression of the power is obtained, which is a function of $Z_{PTO}(\omega) = \left[B_{pto} - j \frac{C_{pto}}{\omega} \right]$. The optimal conditions are obtained by maximizing the expression of P for B_{pto} and C_{pto} . Observing Equation (9), it is obvious that B_{pto} can only be positive, whereas C_{pto} can also be negative. Through varying B_{pto} and C_{pto} for each frequency and wave height, it is easy to find the conditions that give the maximum power. A contour plot for a reference frequency of 1 Hz, $H = 0.1$ m, is shown in Figure 15: although the incident energy is 11.1 W, the maximum that can be extracted is 7.09 W. Given that the geometrical scale is 1:20, this production is equivalent to an average power of 250 kW for a 20 m long module with incident wave $H = 2.0$ m and period $T = 4.5$ s. It is noted that the optimal B_{pto} and C_{pto} and the relative maximum power vary with frequency in a continuous manner, although the derivative is discontinuous under resonance conditions.

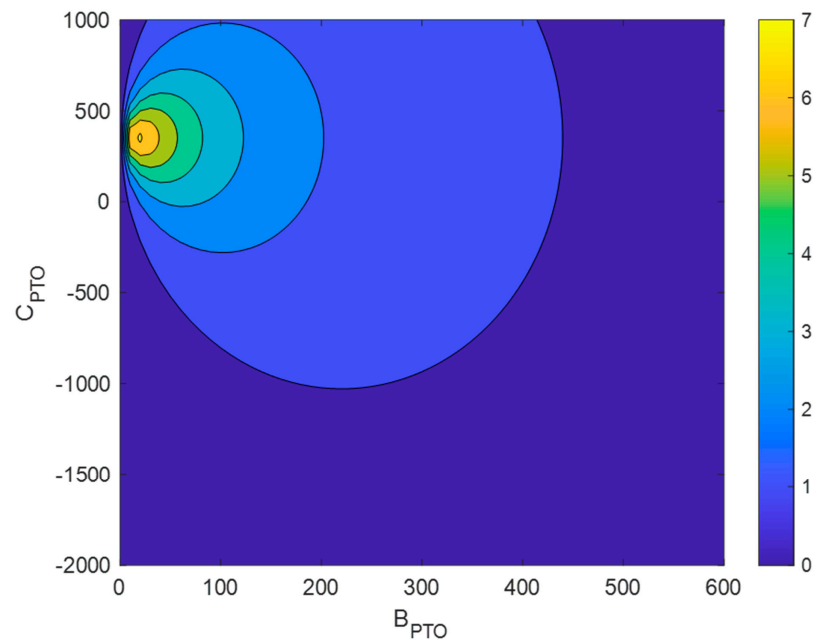


Figure 15. Extracted power in Watts evaluated for a frequency of 1 Hz, assuming $H = 0.1$ m, as a function of B_{pto} and C_{pto} (see Equation (9)). The maximum value is 7.09 W.

Figure 16b shows the optimal power for all frequencies, evaluated assuming the theoretical (BIEM) values of system impedance. It can be observed that the selected

“optimal” B_{pto} and C_{pto} are continuous, with B_{pto} ranging from 10 to 40 Ns/m and C_{pto} ranging from approximately -1200 to 800 N/m (Figure 16a). Efficiency drops after 1.5 Hz to values lower than 20%.

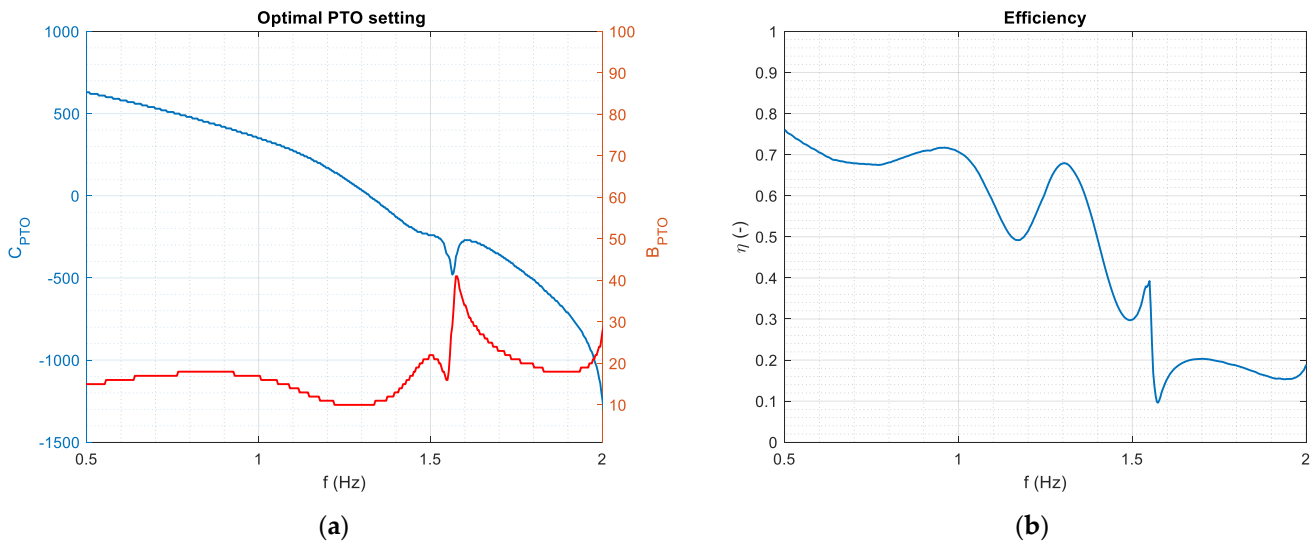


Figure 16. (a) Optimal PTO settings and (b) maximum efficiency.

Figure 17b shows the maximum power production using the actual experimental results. In this second case, where the nonlinear effects are implicit in the measurements, the results depend on the amplitude of the forced oscillation tests. The selected “optimal” B_{pto} and C_{pto} (Figure 17a) are not significantly dependent on the amplitude of the oscillation, but the efficiency is clearly lower for larger oscillations. The case with lower amplitude is, as expected, closer to the theoretical linear case.

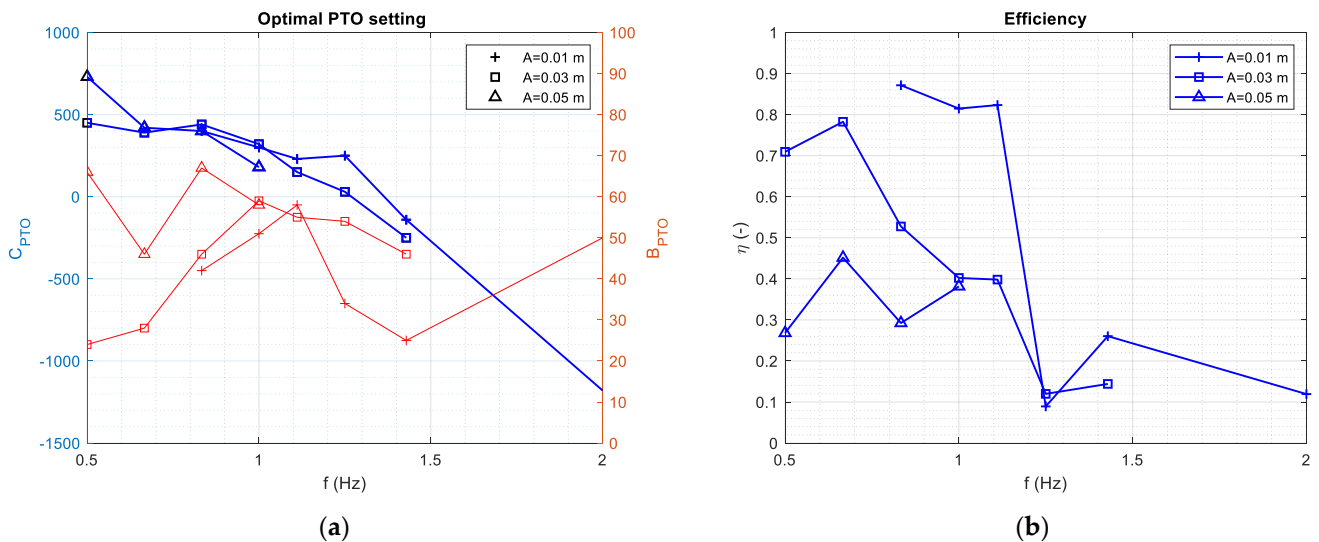


Figure 17. Experimental (a) PTO settings and (b) maximum efficiency.

In conclusion, Figure 17b shows that the efficiency is far from 100% and, for some frequency ranges, it is very limited. This type of result is device-dependent and can significantly support the development process of the device if the relevant analysis is carried out during an early stage of the design.

The aforementioned results should also be considered during the assessment of the potential impact of wave energy harvesting potential, since, in some cases, the approach is

too optimistic. The values still do not account for the losses in the electrical machine, which further reduce the efficiency by approximately 10%.

Finally, other important parameters for monitoring the PTO control strategy are found and given in Figure 18. At optimal values of B_{pto} and C_{pto} , the optimal velocity (Equation (10)) is found, and hence the phase shift between velocity and vertical excitation force. It should be noticed that the phase shift is far from zero, which is the expected shift at the resonance conditions of a single DoF system (e.g., a heaving buoy).

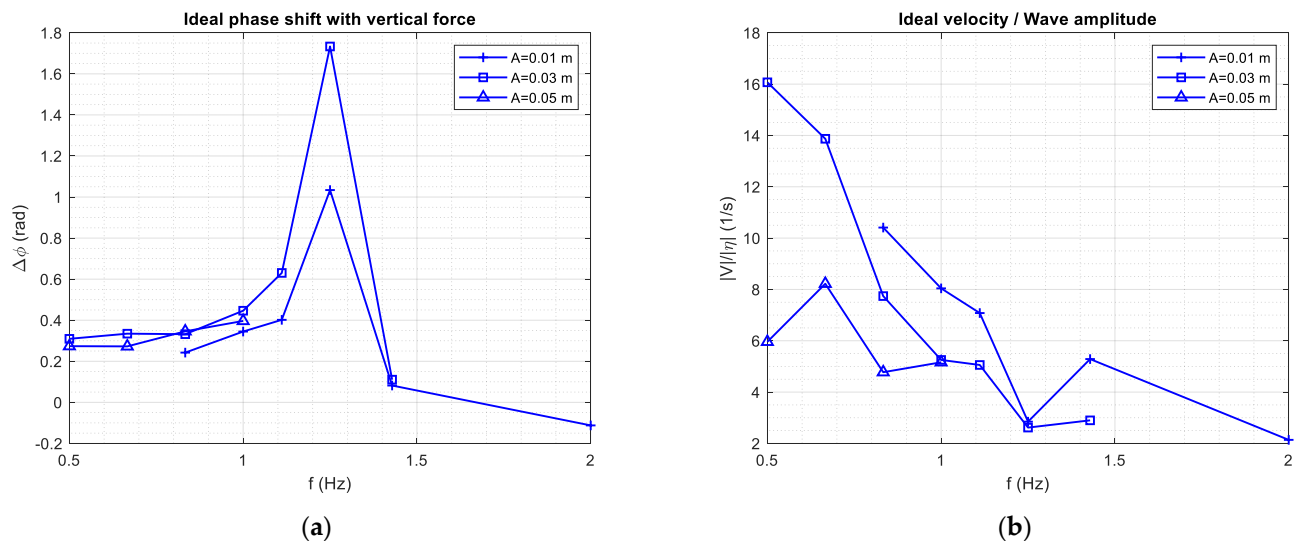


Figure 18. Optimal phase shift between (a) force and velocity and (b) optimal amplitude of the velocity for different experimental A values (see Table 3).

6. Conclusions

The paper presents the “Wave Attenuator”, a hybrid TRL 4 wave-activated body device, installed over a floating breakwater with a moonpool, moored with piles. The main purpose of the structure is protecting a marina; it has two degrees of freedom, pitch and heave; and a PTO is installed on one extreme of each module of the floating breakwater. It is intended for mild wave climates (peak period lower than 4 to 5 s and a maximum significant wave height of 1.5 m), and the harvesting potential is only secondary. The aim of this research is to achieve an experimental proof of the actual efficiency, considering the real interactions between the waves and PTO at the laboratory scale.

For floating WECs, the maximum efficiency limit can be found using a simple formula based on the knowledge of the mechanical impedance $Z(\omega)$. Such a limit is important for economic considerations but is frequently unavailable. Using the “wave attenuator” as an example case, it is shown how it is possible to evaluate $Z(\omega)$ experimentally in order to obtain a realistic value of the maximum efficiency. The estimated value was significantly lower than the efficiency based on the evaluation of $Z(\omega)$ using a model based on linear potential theory.

More specifically, it was found that, at the model scale, efficiency is high only below 1.5 Hz. The maximum value obtained through the numerical approach (WAMIT) decreases from 70% at 0.5 Hz, to 20% at 1.5 Hz. The experimental investigation shows that when the power production is significant (large oscillations), the maximum efficiency is even lower, approximately 50%, with a dependence on the frequency range similar to that in the modeled conditions.

This study supports the importance of a co-design approach and, in particular, an early inclusion of the PTO design together with small-scale hydraulic tests.

Further research is planned to improve the settings for the PTO control strategy during specific tests where the PTO settings are modified, starting from the initial values given in Figure 18. It will also be possible to verify and validate the predicted values, at optimal

conditions, of the phase lag between the PTO force and the velocity, and of the intensity (modulus) of the velocity.

Author Contributions: Conceptualization, L.M., C.F., M.V., P.R. and M.A.; methodology, L.M. and M.A.; software, L.M., G.C., E.L. and M.A.; writing—original draft preparation, L.M.; writing—review and editing, L.M., C.F. and E.L.; experimental activity: L.M., G.C., M.V. and M.A. All authors have read and agreed to the published version of the manuscript.

Funding: This research was funded by the Centro studi di Economia e Tecnica dell’Energia Giorgio Levi Cases, Università degli Studi di Padova, Italy, by PNRR MUR—M4C2—Investimento 1.3—Extended Partnership—“NEST”—Intervention area “2—Future energy scenarios” (Id. Code PE00000021),—Spoke 5 “Energy conversion” CUP C93C22005230007.

Data Availability Statement: The data presented in this study are available on request from the corresponding author.

Acknowledgments: This work is dedicated to the memory of late Prof. Andrea Tortella, who participated in the invention and development of the Wave Attenuator concept.

Conflicts of Interest: The authors declare no conflict of interest.

References

1. Foteinis, S. Wave energy converters in low energy seas: Current state and opportunities. *Renew. Sustain. Energy Rev.* **2022**, *162*, 112448. [CrossRef]
2. Hutchings, J. Brevet de 15 ans. Appareil Produisant de la Force Motrice par L’Utilisation du Mouvement des Marées et des Vagues. Représenté par Rinay, rue de Provence n. 59, Paris, France. 29 November 1905. Available online: [https://patents.google.com/patent/FR359932A/fr?q=\(Appareil+produisant+de+la+force+motrice+par+l%E2%80%99utilisation+du+mouvement+des+mar%C3%A9es+et+des+vagues\)&oq=Appareil+produisant+de+la+force+motrice+par+l%E2%80%99utilisation+du+mouvement+des+mar%C3%A9es+et+des+vagues](https://patents.google.com/patent/FR359932A/fr?q=(Appareil+produisant+de+la+force+motrice+par+l%E2%80%99utilisation+du+mouvement+des+mar%C3%A9es+et+des+vagues)&oq=Appareil+produisant+de+la+force+motrice+par+l%E2%80%99utilisation+du+mouvement+des+mar%C3%A9es+et+des+vagues) (accessed on 29 October 2023).
3. Iardella, E.; Giacchi, M. (Melchiorre) Improvements in Wave Actuated Motors. Filed to United Kingdom. Expired, Patent n. GB202709A, 20 May 1922. Available online: [https://patents.google.com/patent/GB202709A/en?q=\(%22Improvements+in+Wave+Actuated+Motors%22\)&oq=%22Improvements+in+Wave+Actuated+Motors%22](https://patents.google.com/patent/GB202709A/en?q=(%22Improvements+in+Wave+Actuated+Motors%22)&oq=%22Improvements+in+Wave+Actuated+Motors%22) (accessed on 29 October 2023).
4. Clemente, D.; Rosa-Santos, P.; Taveira-Pinto, F. On the potential synergies and applications of wave energy converters: A review. *Renew. Sustain. Energy Rev.* **2021**, *135*, 110162. [CrossRef]
5. Offshore Renewable Energy. Available online: https://energy.ec.europa.eu/topics/renewable-energy/offshore-renewable-energy_en (accessed on 22 October 2023).
6. Zhao, X.; Du, X.; Li, M.; Götteman, M. Semi-analytical study on the hydrodynamic performance of an interconnected floating breakwater-WEC system in presence of the seawall. *Appl. Ocean Res.* **2021**, *109*, 102555. [CrossRef]
7. Falcão, A.F.d.O. Wave energy utilization: A review of the technologies. *Renew. Sustain. Energy Rev.* **2010**, *14*, 899–918. [CrossRef]
8. Pecher, A.; Kofoed, J.P. (Eds.) *Handbook of Ocean Wave Energy*; Softcover reprint of the original 1st edition 2017; Springer International Publishing: Cham, Switzerland, 2018; ISBN 978-3-319-81990-7.
9. Pecher, A.; Kofoed, J.; Espedal, J.; Hagberg, S. Results of an Experimental Study of the Langlee Wave Energy Converter. In Proceedings of the International Offshore and Polar Engineering Conference, Beijing, China, 20–25 June 2010; Volume 1, pp. 877–885.
10. Savin, A.; Salar, D.; Hultman, E. Low-RPM Torque Converter (LRTC). *Energies* **2021**, *14*, 5071. [CrossRef]
11. Falcão, A.F.d.O. Phase control through load control of oscillating-body wave energy converters with hydraulic PTO system. *Ocean Eng.* **2008**, *35*, 358–366. [CrossRef]
12. Peretta, S.; Ruol, P.; Martinelli, L.; Tetu, A.; Kofoed, J. Effect Of a negative stiffness mechanism on the performance of the WEPTOS rotors. In *MARINE 2015—Computational Methods in Marine Engineering VI*; CIMNE: Barcelona, Spain, 2015; pp. 58–72.
13. Martinelli, L.; Volpato, M.; Favaretto, C.; Ruol, P. Hydraulic Experiments on a Small-Scale Wave Energy Converter with an Unconventional Dummy Pto. *Energies* **2019**, *12*, 1218. [CrossRef]
14. Ning, D.; Zhao, X.; Götteman, M.; Kang, H. Hydrodynamic performance of a pile-restrained WEC-type floating breakwater: An experimental study. *Renew. Energy* **2016**, *95*, 531–541. [CrossRef]
15. Coe, R.G.; Bacelli, G.; Forbush, D. A practical approach to wave energy modeling and control. *Renew. Sustain. Energy Rev.* **2021**, *142*, 110791. [CrossRef]
16. Wilson, D.G.; Robinett, R.D.; Bacelli, G.; Abdelkhalik, O.; Coe, R.G. Extending Complex Conjugate Control to Nonlinear Wave Energy Converters. *JMSE* **2020**, *8*, 84. [CrossRef]
17. Haider, A.S.; Brekken, T.K.A.; Coe, R.G.; Bacelli, G.; McCall, A. On Real-Time Hybrid Testing of Ocean Wave Energy Conversion Systems: An Experimental Study. *IEEE Open J. Ind. Applicat.* **2022**, *3*, 30–40. [CrossRef]
18. Bacelli, G.; Coe, R.; Patterson, D.; Wilson, D. System Identification of a Heaving Point Absorber: Design of Experiment and Device Modeling. *Energies* **2017**, *10*, 472. [CrossRef]

19. Ferri, F.; Ambühl, S.; Fischer, B.; Kofoed, J.P. Balancing Power Output and Structural Fatigue of Wave Energy Converters by Means of Control Strategies. *Energies* **2014**, *7*, 2246–2273. [[CrossRef](#)]
20. Fusco, F.; Ringwood, J.V. Short-Term Wave Forecasting for Real-Time Control of Wave Energy Converters. *IEEE Trans. Sustain. Energy* **2010**, *1*, 99–106. [[CrossRef](#)]
21. Montoya, D.; Tedeschi, E.; Castellini, L.; Martins, T. Passive Model Predictive Control on a Two-Body Self-Referenced Point Absorber Wave Energy Converter. *Energies* **2021**, *14*, 1731. [[CrossRef](#)]
22. Martinelli, L.; Ruol, P.; Favaretto, C. Hybrid structure combining a wave energy converter and a floating breakwater. In Proceedings of the 26th International Ocean and Polar Engineering Conference, Rhodes, Greece, 26 June–1 July 2016; Volume 1, pp. 622–628.
23. Burcharth, H.F.; Zanuttigh, B.; Andersen, T.L.; Lara, J.L.; Steendam, G.J.; Ruol, P.; Sergent, P.; Ostrowski, R.; Silva, R.; Martinelli, L.; et al. Innovative Engineering Solutions and Best Practices to Mitigate Coastal Risk. In *Coastal Risk Management in a Changing Climate*; Butterworth-Heinemann: Oxford, UK, 2014; pp. 55–170. ISBN 978-0-12-397331-3.
24. Neshat, M.; Mirjalili, S.; Sergiienko, N.Y.; Esmailzadeh, S.; Amini, E.; Heydari, A.; Garcia, D.A. Layout optimisation of offshore wave energy converters using a novel multi-swarm cooperative algorithm with backtracking strategy: A case study from coasts of Australia. *Energy* **2022**, *239*, 122463. [[CrossRef](#)]
25. Neshat, M.; Sergiienko, N.Y.; Mirjalili, S.; Majidi Nezhad, M.; Piras, G.; Astiaso Garcia, D. Multi-Mode Wave Energy Converter Design Optimisation Using an Improved Moth Flame Optimisation Algorithm. *Energies* **2021**, *14*, 3737. [[CrossRef](#)]
26. Esmailzadeh, S.; Alam, M.-R. Shape optimization of wave energy converters for broadband directional incident waves. *Ocean Eng.* **2019**, *174*, 186–200. [[CrossRef](#)]
27. Andriollo, M.; Lax, E.; Tortella, A.; Martinelli, L. Control strategy for the maximum power extraction of a wave attenuator. In Proceedings of the 2022 Second International Conference on Sustainable Mobility Applications, Renewables and Technology (SMART), Cassino, Italy, 23–25 November 2022; pp. 1–10.
28. Margheritini, L.; Frigaard, P.; Iglesias, G. Technological and commercial comparison of OWC and SSG wave energy converters built into breakwaters. In *Developments in Renewable Energies Offshore*; Guedes Soares, C., Ed.; CRC Press: Boca Raton, FL, USA, 2020; pp. 167–178. ISBN 978-1-00-313457-2.
29. Dallavalle, E.; Cipolletta, M.; Casson Moreno, V.; Cozzani, V.; Zanuttigh, B. Towards green transition of touristic islands through hybrid renewable energy systems. A case study in Tenerife, Canary Islands. *Renew. Energy* **2021**, *174*, 426–443. [[CrossRef](#)]
30. Simonetti, I.; Cappiotti, L. Mediterranean coastal wave-climate long-term trend in climate change scenarios and effects on the optimal sizing of OWC wave energy converters. *Coast. Eng.* **2023**, *179*, 104247. [[CrossRef](#)]
31. Gao, J.; Lyu, J.; Wang, J.; Zhang, J.; Liu, Q.; Zang, J.; Zou, T. Study on Transient Gap Resonance with Consideration of the Motion of Floating Body. *China Ocean Eng.* **2022**, *36*, 994–1006. [[CrossRef](#)]
32. Gao, J.; He, Z.; Zang, J.; Chen, Q.; Ding, H.; Wang, G. Topographic effects on wave resonance in the narrow gap between fixed box and vertical wall. *Ocean Eng.* **2019**, *180*, 97–107. [[CrossRef](#)]
33. Gao, J.; Zang, J.; Chen, L.; Chen, Q.; Ding, H.; Liu, Y. On hydrodynamic characteristics of gap resonance between two fixed bodies in close proximity. *Ocean Eng.* **2019**, *173*, 28–44. [[CrossRef](#)]
34. Wamit Inc. The State of the Art in Wave Interaction Analysis. Available online: <https://www.wamit.com/> (accessed on 25 October 2023).
35. Lee, C.-H.; Newman, J. Computation of wave effects using the panel method. *WIT Trans. State Art Sci. Eng.* **2005**, *18*, 211–251. [[CrossRef](#)]
36. Kramer, M.B.; Andersen, J.; Thomas, S.; Bendixen, F.B.; Bingham, H.; Read, R.; Holk, N.; Ransley, E.; Brown, S.; Yu, Y.-H.; et al. Highly Accurate Experimental Heave Decay Tests with a Floating Sphere: A Public Benchmark Dataset for Model Validation of Fluid–Structure Interaction. *Energies* **2021**, *14*, 269. [[CrossRef](#)]
37. Peña-Sanchez, Y.; Windt, C.; Davidson, J.; Ringwood, J.V. A Critical Comparison of Excitation Force Estimators for Wave-Energy Devices. *IEEE Trans. Control Syst. Technol.* **2020**, *28*, 2263–2275. [[CrossRef](#)]

Disclaimer/Publisher’s Note: The statements, opinions and data contained in all publications are solely those of the individual author(s) and contributor(s) and not of MDPI and/or the editor(s). MDPI and/or the editor(s) disclaim responsibility for any injury to people or property resulting from any ideas, methods, instructions or products referred to in the content.